

# 3D Fourier-based Global Feature Extraction for Hyperspectral Image Classification

Muhammad Ahmad

**Abstract**—Hyperspectral image classification (HSIC) has been significantly advanced by deep learning methods that exploit rich spatial-spectral correlations. However, existing approaches still face fundamental limitations: transformer-based models suffer from poor scalability due to the quadratic complexity of self-attention, while recent Fourier transform-based methods typically rely on 2D spatial FFTs and largely ignore critical inter-band spectral dependencies inherent to hyperspectral data. To address these challenges, we propose Hybrid GFNet (HGFNet), a novel architecture that integrates localized 3D convolutional feature extraction with frequency-domain global filtering via GFNet-style blocks for efficient and robust spatial-spectral representation learning. HGFNet introduces three complementary frequency transforms tailored to hyperspectral imagery: Spectral Fourier Transform (a 1D FFT along the spectral axis), Spatial Fourier Transform (a 2D FFT over spatial dimensions), and Spatial-Spatial Fourier Transform (a 3D FFT jointly over spectral and spatial dimensions), enabling comprehensive and high-dimensional frequency modeling. The 3D convolutional layers capture fine-grained local spatial-spectral structures, while the Fourier-based global filtering modules efficiently model long-range dependencies and suppress noise. To further mitigate the severe class imbalance commonly observed in HSIC, HGFNet incorporates an Adaptive Focal Loss (AFL) that dynamically adjusts class-wise focusing and weighting, improving discrimination for underrepresented classes. Additionally, an adaptive fully connected classification head enhances flexibility and generalization across datasets with varying class distributions. Extensive experiments on benchmark hyperspectral datasets demonstrate that HGFNet consistently outperforms state-of-the-art methods in terms of accuracy, effectively overcoming the limitations of prior approaches. The source code will be made publicly available on GitHub.

**Index Terms**—Hyperspectral Image Classification, Spatial-Spectral Correlation; Fourier transformation, Adaptive focal loss.

## I. INTRODUCTION

Hyperspectral Image (HSI) Classification (HSIC) is a challenging problem in remote sensing and Earth observation, aiming to assign a semantic land-cover/material label to each pixel by exploiting hundreds of contiguous spectral bands [1], [2]. Unlike RGB imagery, hyperspectral measurements provide dense reflectance signatures that enable fine-grained discrimination among materials with subtle spectral differences [3], [4], which is essential for precision agriculture [5], [6], environmental monitoring [7], [8], mineral exploration [9], [10], and land-use/land-cover mapping [11]. However, HSIC remains challenging due to the intrinsic properties of hyperspectral data: extremely high dimensionality, strong inter-band

correlation (spectral redundancy), and complex spatial heterogeneity [12], [13]. The “curse of dimensionality” manifests in two coupled ways: (i) the effective sample complexity increases rapidly with the feature dimension, and (ii) redundant and noisy bands can dominate learning when labeled samples are limited, which increases the risk of overfitting and unstable decision boundaries [14]. In practical scenarios, the difficulty is further amplified by scarce and imbalanced annotations, since ground truth acquisition requires expensive field surveys and expert interpretation [15], [16], while classes often exhibit high inter-class spectral similarity (e.g., vegetation species) and large intra-class variability induced by illumination [17], [18], atmospheric effects, phenological stages, and mixed pixels [19], [20].

Deep learning has substantially advanced HSIC by learning hierarchical spatial-spectral features directly from data [21], with 3D convolutional neural networks (3D CNNs) and transformers emerging as two dominant paradigms [22]. 3D CNNs are effective because their kernels jointly convolve across spatial neighborhoods and spectral bands, thereby encoding local spectral gradients, local texture, and neighborhood context in a unified manner [23]. This local inductive bias is particularly valuable for hyperspectral imagery, where small spatial structures and local mixing patterns can disambiguate classes with similar spectra [24]. Nevertheless, 3D CNNs can be computationally expensive and memory intensive, and their locality limits the receptive field unless deeper stacks or larger kernels are used, which often increases the number of parameters and exacerbates the dependence on larger labeled datasets for stable generalization [25].

Transformers, in contrast, are attractive due to their ability to capture long-range dependencies through self-attention, enabling global context aggregation that improves spatial consistency and class boundary delineation [26]–[28]. Recent hybrid designs attempt to reduce transformer overhead while retaining global modeling capacity, such as MSC-3DLT, which combines multi-scale convolutional extraction with lightweight transformer modules [29], and SSFBF, which couples CNN and transformer components via dynamic routing attention to enhance high-resolution spatial-spectral semantics [30]. Despite these advances, transformer-based HSIC pipelines can still be constrained by the quadratic attention cost and by the difficulty of scaling to high-dimensional spectral inputs without careful tokenization and dimensionality reduction.

Beyond these mainstream approaches, several works incorporate specialized mechanisms to balance local detail and global context. For example, SClusterFormer introduces spatial-spectral cluster attention and deformable convolutions to adaptively model fine-grained structures, though its robust-

M. Ahmad is with SDAIA-KFUPM, Joint Research Center for Artificial Intelligence (JRCAI), King Fahd University of Petroleum and Minerals, Dhahran, 31261, Saudi Arabia. (e-mail: mahmad00@gmail.com).

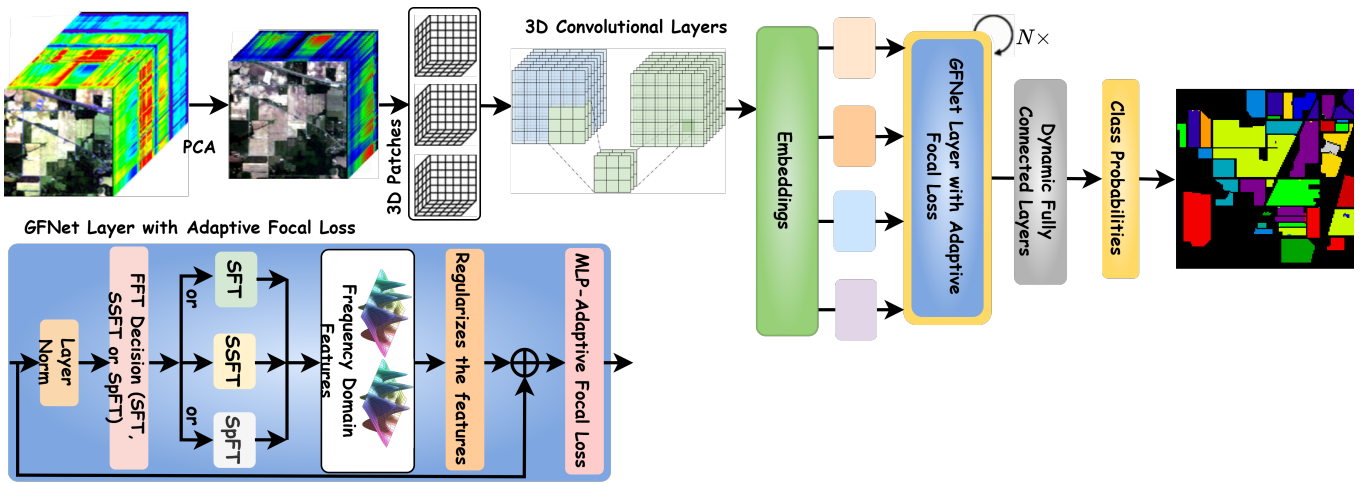


Fig. 1: HSI cubes are first divided into 3D patches to preserve local and contextual dependencies. Three consecutive 3D Convolutional layers extract hierarchical features, while the GFNet layer enhances representations by transforming spatial-spectral data into the frequency domain. After normalization, a 3D FFT decomposes features into frequency components, where learnable global filters emphasize relevant information and suppress noise. The transformed features undergo regularization and pass through a Multilayer perceptron (MLP) block with AFL to handle class imbalances. A residual connection ensures stable gradient flow and feature preservation before dynamic fully connected layers generate the final class probabilities.

ness can be affected by dataset-dependent spectral resolution, sensor noise, and the stability of clustering under limited annotations [31]. MCTGCL integrates CNNs, transformers, and graph contrastive learning for planetary HSIC, offering strong accuracy with reduced complexity, but challenges such as domain shift, limited labels, and generalization across acquisition conditions remain significant [32]. These limitations motivate exploring alternative representations and operators that can provide efficient global interactions with strong inductive priors suited to hyperspectral data.

Frequency-domain learning has recently emerged as a promising direction to complement and replace attention-based global modeling. In particular, Fourier transform-based operators can provide global receptive fields with favorable computational complexity by leveraging the Fast Fourier Transform (FFT), typically  $\mathcal{O}(n \log n)$ , compared to the  $\mathcal{O}(n^2)$  complexity of full self-attention over  $n$  tokens [33]. The Global Frequency Network (GFNet) exploits FFT-based global filtering to enhance robustness to noise and distortions by modulating representations in the frequency domain [34], [35]. However, when directly applied to hyperspectral imagery, many existing frequency-based designs perform FFT primarily over spatial dimensions and treat spectral channels as static features, which can underutilize the most discriminative aspect of hyperspectral data: inter-band spectral correlation and wavelength-dependent frequency structure. Moreover, hyperspectral datasets commonly exhibit severe class imbalance, where minority classes have very few labeled pixels and are easily dominated during optimization; despite its practical importance, relatively few HSIC architectures incorporate principled loss designs that explicitly adapt training dynamics to such imbalance.

To address these challenges, this work proposes Hybrid GFNet (HGFNet), a novel architecture that couples

a lightweight 3D convolutional stem for localized spatial-spectral feature extraction with GFNet-inspired frequency-domain global filtering to jointly learn local and global representations. The design is motivated by a key observation: hyperspectral discrimination requires both (i) local neighborhood evidence to resolve mixed pixels and boundary ambiguity, and (ii) global context to enforce spatial consistency and capture long-range structural dependencies. First, to overcome the limited spectral modeling of prior frequency-based methods, HGFNet introduces a high-dimensional Fourier generalization tailored to hyperspectral inputs. Specifically, we define three complementary transforms: Spectral Fourier Transform (SFT), a 1D FFT along the spectral axis to encode wavelength-wise frequency variations and inter-band dependencies; Spatial Fourier Transform (SpFT), a 2D FFT over spatial dimensions to capture global spatial patterns and long-range correlations; and Spatial-Spectral Fourier Transform (SSFT), a 3D FFT jointly across spatial and spectral dimensions to model coupled frequency structures that arise from the interaction between material spectra and spatial organization. These operators are embedded within GFNet-style blocks and equipped with learnable frequency masks that adaptively modulate frequency components, enabling the network to suppress high-frequency noise while preserving discriminative structures relevant for classification.

Second, HGFNet performs hybrid local-global feature fusion by combining low-level spatial-spectral cues extracted via 3D convolutions with global frequency-aware features produced by Fourier filtering. This coupling provides a stronger inductive bias than using either mechanism alone: the 3D CNN stabilizes learning under limited labels by enforcing locality and spectral continuity, whereas Fourier filtering offers efficient global mixing that improves large-region coherence and reduces patch-level fragmentation. Third, to explicitly

address class imbalance, HGFNet incorporates an Adaptive Focal Loss (AFL) that dynamically adjusts class-wise weighting and focusing behavior. Unlike standard focal loss, which uses a global focusing parameter, AFL adapts the focusing strength per class based on class frequency, thereby emphasizing minority and hard samples without excessively down-weighting well-represented classes. This adaptive optimization strategy complements the proposed frequency-aware representation by improving decision boundaries for underrepresented categories, which is critical for reliable HSIC performance in real-world imbalanced settings. In a nutshell, HGFNet is designed to bridge the gap between local spatial-spectral modeling and efficient global dependency capture by introducing hyperspectral-specific high-dimensional Fourier operators, a principled local-global fusion strategy, and an imbalance-aware adaptive loss enabling robust HSIC.

## II. PROPOSED METHODOLOGY

Let  $\mathbf{X} \in \mathcal{R}^{B \times C \times D \times H \times W}$  be the input HSI data, where  $B$  is the batch size,  $C$  is the number of spectral channels,  $D$  is the depth, and  $H$  and  $W$  are the spatial height and width of the patches. The goal is to learn a function  $f: \mathbf{X} \rightarrow \mathbf{Y}$ , where  $\mathbf{Y} \in \mathcal{R}^{B \times N}$  represents the class probabilities for  $N$  land cover classes as shown in Fig. 1. A 3D convolutional module is applied to capture the spatial-spectral dependencies as:

$$\mathbf{X}' = \sigma(\mathbf{W} \circledast \mathbf{X} + b) \quad (1)$$

where  $\mathbf{W} \in \mathcal{R}^{F \times C \times D_k \times H_k \times W_k}$  represents the 3D convolutional filter, with  $F$  denoting the number of output feature maps,  $D_k$ ,  $H_k$ , and  $W_k$  being the kernel sizes in the spectral and spatial dimensions. The convolution operation  $\circledast$  extracts hierarchical features across spectral-spatial domains. The term  $b \in \mathcal{R}^F$  represents the bias, and  $\sigma$  is the Gaussian error linear unit (GeLU) activation function  $\sigma(x) = x \cdot \Phi(x)$ , where  $\Phi(x)$  is the standard Gaussian cumulative distribution function. This activation function helps preserve fine-grained spectral-spatial information. The convolution operation is performed twice to refine feature representations while maintaining coherence.

### A. GFNet Block

The GFNet block leverages frequency-domain representations to efficiently capture long-range dependencies. By employing the 3D-FFT, the spatial-spectral features are decomposed into frequency components, enabling effective feature selection and transformation. Prior to the FFT, feature normalization is applied to stabilize numerical computations and enhance convergence as:

$$X_{\text{norm}} = \frac{\mathbf{X}' - \mu}{\phi} \quad (2)$$

where  $\mu$  and  $\phi$  denote the mean and standard deviation of the input feature tensor, respectively. The FFT operation transforms the spatial-spectral representation into its frequency-domain equivalent as:

$$\mathbf{X}_{FT} = \mathcal{F}(X_{\text{norm}}, \text{backward}) \quad (3)$$

where  $\mathcal{F}$  represents the FFT function computed with backward normalization. The ‘backward’ norm ensures that the transformation does not introduce unintended scaling effects by preserving the correct magnitude of the transformed signal. Unlike ‘ortho’ scaling the forward and inverse transforms by  $1/\sqrt{N}$ , the ‘backward’ normalization guarantees:

$$\mathcal{F}^{-1}(\mathcal{F}(X_{\text{norm}}, \text{backward}), \text{backward}) = X_{\text{norm}} \quad (4)$$

This formulation ensures that the inverse FFT restores the original feature map without additional scaling adjustments, leading to stable feature propagation and improved training performance. To enhance feature extraction, a frequency-domain mask is applied:

$$\mathbf{X}'_{FT} = \mathbf{X}_{FT} \odot M \quad (5)$$

where  $M$  is a binary mask that selectively retains informative frequency components while suppressing noise and redundant signals. The Hadamard product ( $\odot$ ) ensures element-wise filtering, preserving dominant spectral features. The frequency-transformed features are passed through a feed-forward network (FFN) to capture complex interactions:

$$\mathbf{X}_{FFN} = \sigma(\mathbf{W}_1 \mathbf{X}'_{FT} + b_1) \quad (6)$$

$$\mathbf{X}_{\text{out}} = \mathbf{W}_2 \mathbf{X}_{FFN} + b_2 \quad (7)$$

where  $\mathbf{W}_1 \in \mathcal{R}^{d_h \times d}$  and  $\mathbf{W}_2 \in \mathcal{R}^{d \times d_h}$  are learnable weight matrices, and  $\sigma$  is a non-linearity that enhances feature expressiveness. To prevent information loss and gradient instability, a residual connection is incorporated:

$$\mathbf{X}_{\text{final}} = \mathbf{X}_{\text{norm}} + \mathbf{X}_{\text{out}} \quad (8)$$

This formulation ensures efficient feature aggregation while mitigating vanishing gradient issues. Finally, the refined representation is passed through fully connected layers:

$$\mathbf{Z}_1 = \sigma(\mathbf{W}_3 \mathbf{X}_{\text{final}} + b_3) \quad \& \quad \mathbf{Z}_2 = \sigma(\mathbf{W}_4 \mathbf{Z}_1 + b_4) \quad (9)$$

$$\mathbf{Y} = \text{softmax}(\mathbf{W}_5 \mathbf{Z}_2 + b_5) \quad (10)$$

where  $\mathbf{W}_3, \mathbf{W}_4, \mathbf{W}_5$  are trainable weight matrices, and  $b_3, b_4, b_5$  are bias terms. The final softmax operation converts the output into class probabilities.

### B. AFL and Training

To address the severe class imbalance in hyperspectral datasets, we adapt the AFL proposed in [36], originally designed for natural image classification, to the hyperspectral domain as follows:

$$L = - \sum_{i=1}^N \alpha_i (1 - p_i)^{\gamma_i} \log(p_i) \quad (11)$$

where,  $\alpha_i$  is a class-specific weight accounting for class frequency,  $p_i$  is the predicted softmax probability for class  $i$ ,

and  $\gamma_i$  is a dynamic focusing parameter that emphasizes harder samples. Unlike [36], using globally learned parameters, we define both  $\alpha_i$  and  $\gamma_i$  adaptively per class to reflect the uneven spectral separability and spatial distribution inherent in HSIC tasks. Additionally, our formulation smoothly integrates with frequency-based GFNet blocks, allowing the model to emphasize discriminative spectral features also for underrepresented classes. The training is done by the Adam optimizer as:

$$\theta_{t+1} = \theta_t - \eta \frac{\partial L}{\partial \theta} \quad (12)$$

where  $\eta$  is the learning rate and  $\theta$  represents model parameters.

### III. EXPERIMENTAL SETTINGS AND RESULTS

To demonstrate the proposed HGFNet model’s effectiveness, experiments on three HSI datasets, i.e., Indian Pines (IP), WHU Hi HanChuan (HC), and WHU Hi HongHu (HH) have been performed. The IP dataset is widely used for benchmarking hyperspectral models, whereas the HH and HC datasets provide different real-world scenarios.

The proposed HGFNet is trained using the Adam optimizer with an initial learning rate of 0.001 and a weight decay of  $1 \times 10^{-6}$  to mitigate overfitting and stabilize parameter updates. The network is optimized for 50 epochs with a batch size of 64, which provides a balanced trade-off between convergence stability and computational efficiency. For all experiments, the datasets are randomly partitioned such that 25% of the labeled samples are used for training, 25% for validation to monitor convergence and prevent overfitting, and the remaining 50% are reserved for testing. This split ensures a sufficiently large and unbiased test set, enabling a reliable assessment of generalization performance under limited labeled data, which is a common and challenging setting in HSIC.

The HGFNet consists of several key components designed for effective feature extraction and classification. It begins with three 3D convolutional layers equipped with GELU activation to capture spatial-spectral features. Following this, four GFNet Blocks are employed, integrating FFTs and MLP layers, along with GELU activation, normalization, and dropout, to enhance feature representation. The classification head features a fully connected classifier that is dynamically initialized based on the feature dimensions, incorporating ReLU activations and dropout layers to improve generalization. To address class imbalance, the model utilizes an AFL with class-balanced weighting, ensuring more robust learning across different classes.

#### A. Ablation Study

To rigorously analyze the contribution of each architectural component, we conduct an extensive ablation study focusing on frequency-domain modeling and attention/loss design. The study is designed to answer three key questions: (i) how spatial and spectral frequency components individually contribute to hyperspectral representation learning; (ii) whether joint spatial-spectral frequency modeling yields complementary benefits; and (iii) how the proposed adaptive focal loss (AFL) interacts with frequency-aware representations.

#### a) Impact of Spatial and Spectral Frequency Modeling.:

We first investigate the effect of selectively enabling spatial and spectral Fourier transforms. The SpFT variant retains only spatial FFT, emphasizing periodic structures and texture regularities in the spatial domain, while discarding spectral correlations. Conversely, SFT preserves only spectral FFT, modeling frequency patterns along the wavelength dimension that capture material-specific signatures and subtle spectral variations. The SSFT configuration applies a full 3D FFT, jointly transforming spatial and spectral dimensions to encode long-range dependencies and cross-dimensional frequency interactions.

As reported in Table I, SSFT consistently outperforms both SpFT and SFT across all datasets and metrics. This confirms that spatial and spectral frequency cues are complementary rather than redundant. While spatial frequency information captures structural and contextual patterns, spectral frequency components are critical for discriminating materials with similar spatial appearances but distinct spectral responses. The joint transformation enables the network to model complex couplings between spatial layout and spectral variation, which are otherwise inaccessible when operating in a single domain.

b) *Spectral Dominance in Hyperspectral Data.:* A consistent trend is that SFT slightly outperforms SpFT in terms of  $\kappa$ , OA, and AA on most datasets. This observation aligns well with the nature of hyperspectral imagery, where class separability is largely driven by spectral signatures rather than purely spatial patterns. Frequency analysis along the spectral dimension effectively suppresses noise, enhances discriminative wavelength bands, and captures periodic or smooth spectral behaviors associated with specific land-cover classes. Nevertheless, the performance gap between SFT and SSFT highlights that spectral modeling alone is insufficient, and that spatial frequency context remains essential for robust classification.

c) *Comparison with Attention and Other Frequency-Based Baselines.:* Compared to the MHSA baseline, all FFT-based variants demonstrate clear improvements, indicating that explicit frequency-domain modeling provides a stronger inductive bias than attention alone. While MHSA captures global dependencies in the feature space, it lacks an explicit mechanism to disentangle low- and high-frequency components, which are crucial for handling illumination variations, spectral redundancy, and spatial texture complexity.

We further compare SSFT with two representative frequency-domain approaches: Wavelets and GFNet. Although Wavelets introduce multi-scale frequency decomposition and GFNet leverages global filtering, both methods underperform SSFT. This suggests that the proposed 3D FFT formulation is more effective at jointly modeling spatial-spectral correlations, whereas Wavelets rely on fixed basis functions and GFNet primarily emphasizes global spatial filtering without explicitly exploiting spectral frequency structure.

d) *Effect of Loss Design: SFL vs. AFL.:* Finally, we examine the interaction between frequency-aware representations and loss design. Replacing the standard focal loss (SFL) with the proposed AFL consistently yields further gains across all datasets. AFL dynamically adjusts class-wise

emphasis based on training dynamics, which synergizes well with SSFT features that already enhance class separability in the frequency domain. This combination is particularly beneficial for addressing class imbalance and hard-to-classify samples, leading to more stable optimization and improved generalization.

TABLE I: Quantitative comparison of different frequency and attention-based configurations, including SFL (SFL + SSFT) and the proposed AFL (AFL + SSFT).

Data	Metric	MHSA	Wavelets	GFNet	SpFT	SFT	SFL	AFL
IP	$\kappa$	96.21	97.06	94.22	97.26	97.66	97.92	<b>98.24</b>
	OA	96.68	98.46	92.14	97.60	97.95	96.11	<b>98.45</b>
	AA	95.05	95.69	93.67	96.47	96.35	96.78	<b>97.16</b>
HC	$\kappa$	97.49	95.51	95.73	97.75	97.83	98.67	<b>99.10</b>
	OA	97.85	97.38	96.48	98.07	98.15	98.87	<b>99.23</b>
	AA	95.75	97.76	94.12	96.73	96.44	97.92	<b>98.71</b>
HH	$\kappa$	97.87	96.28	95.91	98.22	98.75	98.96	<b>99.13</b>
	OA	98.31	97.71	96.89	98.59	99.01	97.14	<b>99.31</b>
	AA	96.53	96.64	95.02	96.76	97.97	96.12	<b>98.29</b>

In a nutshell, the ablation results demonstrate that joint SSFT is crucial for maximizing HSIC performance, as it effectively captures complementary spatial structures and discriminative spectral patterns. While spectral frequency information plays a dominant role due to the intrinsic characteristics of hyperspectral data, spatial frequency cues remain essential for providing contextual and structural support. Furthermore, FFT-based modeling consistently outperforms attention-only mechanisms and alternative frequency-domain baselines, indicating the advantage of explicitly disentangling and exploiting frequency components. Finally, the proposed AFL further amplifies these gains when coupled with SSFT by improving class-wise optimization and robustness to hard samples. As a result, AFL + SSFT achieves the best overall performance, reaching 99.13  $\kappa$  and 99.31 OA on the HH dataset, thereby validating the effectiveness of the proposed design.

*B. Experimental Results and Discussion*

To validate the effectiveness of the proposed HGFNet, we conduct extensive experiments on three benchmark hyperspectral datasets and compare against a diverse set of recent state-of-the-art methods, including SpectralFormer [37], Hybrid ViT (HViT) [38], Wavelet-based spatial-spectral transformer (WaveFormer) [27], wavelet-based spatial-spectral Mamba (WaveMamba) [39], and Spatial-spectral Mamba [40]. All methods are trained and evaluated under the same experimental protocol on a single RTX 4060 GPU (8GB VRAM) with 64GB RAM. The goal of this comparative study is to assess not only accuracy (Overall accuracy (OA), Average accuracy (AA), and Kappa coefficient ( $\kappa$ )) but also the robustness of spatial structures and class boundaries in the predicted maps, thereby highlighting the benefits of combining local 3D CNN inductive biases with global Fourier-domain feature mixing in a unified framework.

Table II summarizes the class-wise accuracies and overall metrics on the HC dataset. HGFNet achieves the best overall performance with an OA of 99.2373%, AA of 98.7168%, and  $\kappa$  of 99.1074%, outperforming all competitors across nearly all classes. The performance gain is especially pronounced in classes where strong spectral similarity and intra-class

TABLE II: Class-wise accuracy and overall performance metrics on HC Dataset.

Class	SF	HViT	WFormer	Mamba	WMamba	HGFNet
1	98.4307	99.3383	98.4755	96.9197	96.0255	99.7183
2	99.2001	98.1629	99.2528	83.8006	96.0007	99.6396
3	94.3807	98.6000	85.4754	78.0283	94.8668	99.7472
4	99.8879	99.5517	97.9454	95.6294	99.2528	99.7385
5	97.8333	99.1666	97.1666	73.0000	63.8333	99.6666
6	92.6301	86.4518	81.5975	35.3045	76.8314	96.1606
7	97.7303	94.9186	98.4078	88.5501	95.0203	99.9322
8	94.8492	95.0606	96.9073	76.1820	93.5254	98.5426
9	96.1765	98.2044	97.8876	57.0553	89.5014	98.0566
10	99.4674	98.5545	99.4294	93.7618	95.2073	99.9239
11	97.7764	98.8290	97.6818	79.5742	96.0023	96.4163
12	84.2934	96.7934	95.4347	58.0978	65.4347	99.5108
13	93.7033	90.3905	94.5809	56.6037	72.9486	97.6305
14	98.2974	98.2112	98.6206	74.2780	95.6465	99.2564
15	87.6760	86.4436	90.1408	62.5000	68.4859	95.5985
16	99.6923	99.4111	99.8779	99.1644	98.9177	99.9310
<b><math>\kappa</math></b>	97.4911	97.6654	97.3873	83.9145	93.6020	<b>99.1074</b>
<b>OA</b>	97.8557	98.0048	97.7680	86.3021	94.5280	<b>99.2373</b>
<b>AA</b>	95.7516	96.1305	95.5551	75.5281	87.3438	<b>98.7168</b>

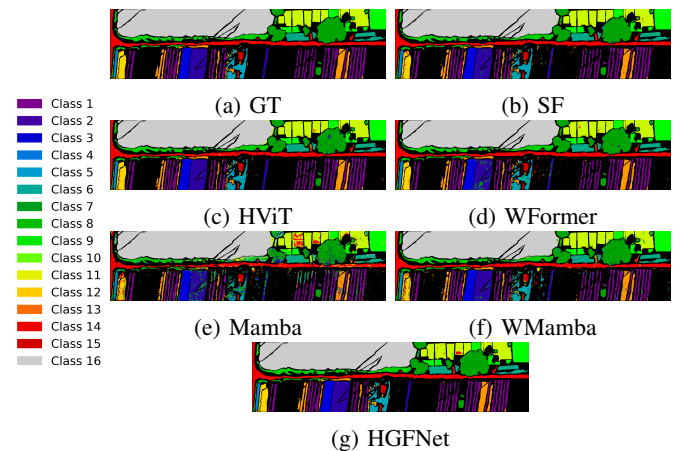


Fig. 2: Visual comparison of classification maps on the HC dataset. (a) Ground truth maps; (b–g) predicted maps from competing models and our proposed HGFNet.

variability typically confuse; in these cases, HGFNet benefits from (i) the local spatial-spectral coupling captured by the 3D CNN front-end, which preserves fine-grained neighborhood context and reduces salt-and-pepper noise, and (ii) the global frequency mixing, which aggregates long-range dependencies and harmonizes globally consistent structures. In contrast, the pure Mamba baseline shows the weakest overall performance (OA 86.3021%,  $\kappa$  83.9145), suggesting that a sequence-modeling bias alone may be insufficient to reliably capture the complex joint spatial-spectral statistics in this dataset, particularly under limited labeled samples and pronounced class imbalance. The qualitative maps in Fig. 2 further corroborate these quantitative trends: HGFNet produces more spatially coherent regions with clearer boundaries and fewer isolated misclassified pixels, indicating that the learned representation is not only discriminative in feature space but also spatially consistent in the image domain.

On the IP dataset (Table III), HGFNet again delivers the strongest overall results, reaching an OA of 98.4583%, AA of 97.1643%, and  $\kappa$  of 98.2419%. IP is known to contain many spectrally similar vegetation classes and fragmented spa-

TABLE III: Class-wise accuracy and overall performance metrics on **IP Dataset**.

Class	SF	HViT	WFormer	Mamba	WMamba	HGFNet
1	95.6521	100	86.9565	4.3478	65.2173	67.3913
2	95.0980	92.5770	93.1372	42.2969	81.5126	95.4481
3	97.1084	96.6265	98.3132	18.0722	77.3493	99.6385
4	94.0677	85.5932	91.5254	3.3898	50.8474	100
5	97.1074	99.5867	98.7603	33.0578	84.7107	97.9296
6	97.8082	98.6301	98.0821	86.5753	87.9452	100
7	85.7142	100	100	0	57.1428	100
8	100	100	100	93.3054	99.5815	100
9	80	90	80	0	60	100
10	90.7407	90.9465	90.7407	33.5390	75.7201	99.8971
11	98.2899	98.7785	98.1270	81.9218	91.2866	98.2484
12	95.9595	96.2962	95.9595	31.3131	69.3602	97.1332
13	98.0392	100	100	46.0784	76.4705	100
14	98.4202	99.2101	98.5781	92.4170	92.8909	99.6837
15	96.8911	97.9274	96.3730	36.2694	73.5751	100
16	100	97.8260	97.8260	54.3478	69.5652	100
$\kappa$	96.2159	96.1922	96.0382	51.1942	81.3875	<b>98.2419</b>
OA	96.6829	96.6634	96.5268	58.3414	83.7268	<b>98.4583</b>
AA	95.0560	96.4999	95.2737	41.0582	75.8235	<b>97.1643</b>

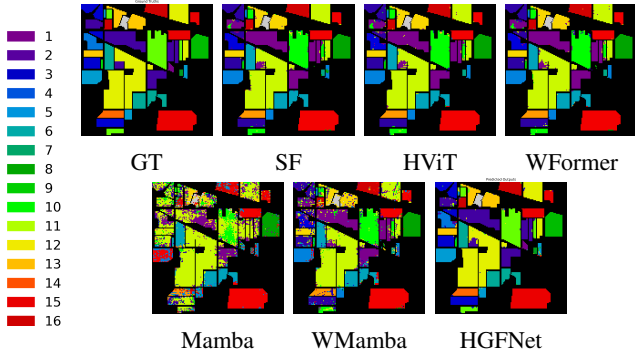


Fig. 3: Predicted ground truth maps for the Indian Pines dataset.

tial distributions, which typically amplify confusion between visually adjacent categories and increase boundary errors. The improvements of HGFNet over transformer-based and wavelet-based baselines suggest that its design is particularly effective at simultaneously addressing (i) local ambiguity, by leveraging 3D convolutions to encode local spatial context together with spectral continuity, and (ii) global context dependency, by using Fourier-domain operations to enable efficient global interactions that stabilize predictions over large homogeneous regions. Although WaveMamba shows a noticeable improvement compared to Mamba, it remains inferior to HGFNet, implying that wavelet decomposition alone does not fully resolve the need for explicit global spatial-spectral coupling. This conclusion is visually supported by Fig. 3, where HGFNet produces more compact and consistent class regions with fewer scattered errors, reflecting stronger structural regularization in the predicted map.

Table IV reports results on the HH dataset, where HGFNet achieves the highest OA (99.3141%),  $\kappa$  (99.1331%), and AA (98.2900%), confirming that the proposed architecture generalizes well across datasets with different spatial resolutions and class compositions. Compared with WaveFormer, which is the next best model in terms of OA, HGFNet yields a higher AA and more stable class-wise performance, indicating improved robustness across both frequent and minority classes.

TABLE IV: Class-wise accuracy and overall performance metrics on **HH Dataset**.

Class	SF	HViT	WFormer	Mamba	WMamba	HGFNet
1	99.4159	99.5584	99.7008	86.8660	95.1709	99.2592
2	93.6788	91.3439	94.9886	64.1799	88.3826	98.9749
3	97.7087	98.5519	99.6333	88.9011	93.3644	99.2484
4	99.7121	98.8033	99.8860	98.8731	99.7427	99.9693
5	91.9588	95.5934	96.1724	79.4467	76.5519	95.2717
6	98.2808	99.5466	99.8967	91.1845	98.9272	99.8788
7	97.1788	97.4278	98.3820	78.3189	87.7862	99.8326
8	89.7385	84.2624	86.9264	31.7217	63.0981	90.6265
9	99.4823	98.9646	97.1898	96.3948	94.3612	99.9075
10	97.4342	98.8058	98.6767	52.2672	87.2357	99.7256
11	98.2204	98.0025	98.2749	68.2585	83.5118	98.0388
12	89.0998	86.6205	93.4331	60.0402	78.2443	98.3247
13	97.8674	95.9747	92.9536	77.0481	83.2237	99.1025
14	97.7705	92.5231	98.5589	86.6503	97.1179	99.6193
15	94.8103	96.6067	99.2015	53.0938	39.9201	98.8023
16	99.5868	99.1462	96.0341	76.5078	95.0151	99.5042
17	96.2126	84.1196	99.1362	82.9900	80.1328	96.4119
18	98.3830	96.5174	94.8383	84.0796	85.0124	95.8333
19	97.8879	97.4288	98.1175	76.1019	90.1974	98.6914
20	96.0986	85.0258	92.7710	34.5381	88.9271	99.5410
21	94.1265	57.0783	70.7831	5.2710	54.3674	99.2469
22	99.2079	97.3762	99.7029	45.9405	93.8118	98.1683
$\kappa$	97.8750	96.8637	98.0616	83.2685	92.3374	99.1331
OA	98.3180	97.5143	98.4664	86.7859	93.9450	99.3141
AA	96.5391	93.1490	95.6935	69.0306	84.2774	98.2900

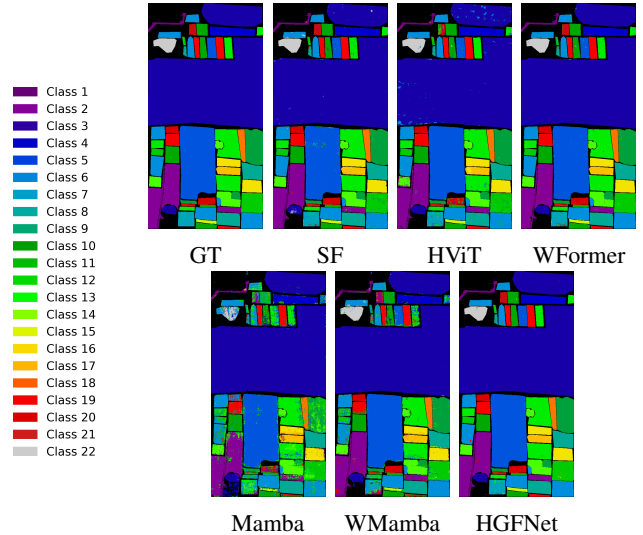


Fig. 4: Predicted ground truth maps for the HH dataset.

Notably, Mamba exhibits severe degradation in several classes (e.g., classes 8, 10, 15, and 21), which substantially lowers AA and reveals instability when discriminative cues require both local neighborhood evidence and globally consistent context. WaveMamba partially mitigates this issue, but still lags behind transformer-based methods and HGFNet, suggesting that combining a sequence model with wavelet priors is beneficial but not sufficient to match the stronger inductive bias produced by explicitly integrating 3D spatial-spectral locality with global Fourier mixing. The qualitative comparison in Fig. 4 is consistent with the metrics: HGFNet generates the cleanest and most spatially consistent map, with reduced boundary fragmentation and fewer misclassification streaks, indicating superior preservation of large-scale structures and more reliable class separation.

Overall, the results across HC, IP, and HH consistently

demonstrate that HGFNet achieves state-of-the-art performance by unifying complementary mechanisms: the 3D CNN backbone captures local spatial-spectral interactions and suppresses pixel-level noise, while Fourier-based global feature extraction enables efficient long-range dependency modeling and improves global consistency. This combination is particularly advantageous in HSIC, where (i) many categories exhibit high spectral correlation, (ii) spatial context is critical for disambiguating mixed pixels and boundary regions, and (iii) limited labeled samples demand strong inductive priors to avoid overfitting. Consequently, HGFNet not only improves OA/ $\kappa$ /AA but also produces visually coherent classification maps with fewer artifacts, supporting its suitability for practical hyperspectral scene understanding.

#### IV. CONCLUSION AND FUTURE RESEARCH DIRECTIONS

This work proposed Hybrid GFNet (HGFNet), a novel hybrid architecture for hyperspectral image classification that explicitly unifies local spatial-spectral modeling with efficient global frequency-domain learning. By integrating a 3D convolutional front-end with GFNet-inspired global Fourier filtering blocks, HGFNet effectively captures fine-grained local structures as well as long-range spatial-spectral dependencies. The introduction of three complementary frequency operators, Spectral Fourier Transform (SFT), Spatial Fourier Transform (SpFT), and Spatial-Spectral Fourier Transform (SSFT), enables high-dimensional frequency modeling tailored to hyperspectral data, allowing the network to exploit inter-band spectral correlations and global spatial patterns simultaneously. In addition, the proposed Adaptive Focal Loss (AFL) explicitly addresses class imbalance by dynamically adjusting class-wise focusing behavior, while the adaptive fully connected classification head improves flexibility and generalization across datasets with diverse class distributions. Extensive experiments on multiple benchmark hyperspectral datasets demonstrate that HGFNet consistently outperforms state-of-the-art methods in terms of overall accuracy, average accuracy, and Cohen's kappa, while also producing more spatially coherent and visually consistent classification maps.

Despite its strong empirical performance, several limitations remain and motivate future research. First, the reliance on Fourier-based global feature extraction inherently assumes signal stationarity, which may limit the model's ability to adapt to highly non-stationary spectral variations caused by complex illumination conditions, atmospheric effects, and sensor noise in real-world hyperspectral imagery. Incorporating adaptive and localized frequency representations, such as learnable spectral bases and hybrid Fourier-wavelet formulations, could improve robustness under such conditions. Second, although the 3D convolutional layers provide strong local inductive biases, their computational and memory costs may hinder scalability to ultra-high-resolution hyperspectral scenes or large-scale datasets. Future work could explore lightweight alternatives, such as depthwise separable 3D convolutions or dynamic kernel decomposition, to further reduce complexity without losing representational power. Finally, while AFL improves performance under moderate class imbalance,

extremely skewed class distributions may require more advanced strategies, such as curriculum-based reweighting, meta-learning of loss functions, or joint sampling-loss optimization. Addressing these challenges will further enhance the practicality and generalization capability of HGFNet, paving the way for robust deployment in large-scale and real-world hyperspectral applications.

#### REFERENCES

- [1] Z. Zhao, X. Xu, S. Li, and A. Plaza, "Hyperspectral image classification using groupwise separable convolutional vision transformer network," *IEEE Transactions on Geoscience and Remote Sensing*, vol. 62, pp. 1–17, 2024.
- [2] F. Ahmad, M. Usama, U. Ghous, D. Shehzad, M. Mazzara, and M. Ahmad, "A spiking and memory-enhanced state-space model for hyperspectral image classification," *IEEE Geoscience and Remote Sensing Letters*, vol. 23, pp. 1–5, 2026.
- [3] B. B. Tulu, F. T. Teshome, Y. Ampatzidis, C. Li, W. Pavan, G. Golmohammadi, and H. K. Bayabil, "Rgb-to-synthetic-thermal image translation using generative ai to support crop water stress assessment," *Computers and Electronics in Agriculture*, vol. 241, p. 111273, 2026. [Online]. Available: <https://www.sciencedirect.com/science/article/pii/S0168169925013791>
- [4] M. Ahmad, F. Mauro, R. A. Raza, M. Mazzara, S. Distefano, A. M. Khan, and S. L. Ullo, "Transformer-driven active transfer learning for cross-hyperspectral image classification," *IEEE Journal of Selected Topics in Applied Earth Observations and Remote Sensing*, vol. 18, pp. 19 635–19 648, 2025.
- [5] A. Karukayil, J. F. Mota, and F. A. Cheein, "3d crop reconstruction: A review of hyperspectral and multispectral approaches," *Computers and Electronics in Agriculture*, vol. 241, p. 111282, 2026. [Online]. Available: <https://www.sciencedirect.com/science/article/pii/S0168169925013882>
- [6] S. Sohail, M. Usama, U. Ghous, M. Mazzara, S. Distefano, and M. Ahmad, "Energyformer: Energy attention with fourier embedding for hyperspectral image classification," *IEEE Geoscience and Remote Sensing Letters*, vol. 22, pp. 1–5, 2025.
- [7] S. Serranti, G. Bonifazi, P. Coccozza, P. Cucuzza, R. Palmieri, M. Benzi, M. Lezzi, C. Mazziotti, E. Riccardi, E. Barbieri, I. Ingrandio, and F. Moroni, "Comparison of hyperspectral imaging and fur spectroscopy for microplastic polymer identification: Proposal of a scalable protocol validated in a 12-month river survey," *Talanta*, p. 129361, 2026. [Online]. Available: <https://www.sciencedirect.com/science/article/pii/S0039914026000147>
- [8] S. Sohail, M. Usama, U. Ghous, M. Mazzara, and M. Ahmad, "Differential attention with enhanced squeeze-and-excitation for hyperspectral image classification," *IEEE Geoscience and Remote Sensing Letters*, vol. 22, pp. 1–5, 2025.
- [9] H. Lkhaoua, O. Raji, A. Elghali, A. E. Alaoui EL Fels, M. Mazigh, and M. Benzaazoua, "Proximal mapping of carbonate-fluorapatite using hyperspectral imaging with sem-eds mineralogical validation: a drill core case study from the ben guerir mine, morocco," *Minerals Engineering*, vol. 237, p. 109997, 2026. [Online]. Available: <https://www.sciencedirect.com/science/article/pii/S0892687525008258>
- [10] M. Ahmad, M. Mazzara, S. Distefano, A. M. Khan, and X. Wu, "Self-supervised spatial-spectral transformer with extreme learning machine for hyperspectral image classification," *International Journal of Remote Sensing*, vol. 46, no. 14, pp. 5384–5407, 2025. [Online]. Available: <https://doi.org/10.1080/01431161.2025.2520049>
- [11] R. Ming, N. Chen, J. Peng, W. Sun, and Z. Ye, "Semantic tokenization-based mamba for hyperspectral image classification," *IEEE Journal of Selected Topics in Applied Earth Observations and Remote Sensing*, vol. 18, pp. 4227–4241, 2025.
- [12] M. Ahmad, M. Mazzara, S. Distefano, A. M. Khan, and S. L. Ullo, "Diffformer: A differential spatial-spectral transformer for hyperspectral image classification," *IEEE Journal of Selected Topics in Applied Earth Observations and Remote Sensing*, vol. 18, pp. 10 419–10 428, 2025.
- [13] L. Chen, J. He, H. Shi, J. Yang, and W. Li, "Swdiff: Stage-wise hyperspectral diffusion model for hyperspectral image classification," *IEEE Transactions on Geoscience and Remote Sensing*, vol. 62, pp. 1–17, 2024.

- [14] M. Ahmad, S. Distefano, A. M. Khan, M. Mazzara, C. Li, H. Li, J. Aryal, Y. Ding, G. Vivone, and D. Hong, "A comprehensive survey for hyperspectral image classification: The evolution from conventional to transformers and mamba models," *Neurocomputing*, vol. 644, p. 130428, 2025. [Online]. Available: <https://www.sciencedirect.com/science/article/pii/S0925231225011002>
- [15] M. Ahmad, M. Mazzara, S. Distefano, and A. M. Khan, "Byte latent mamba with state space and knowledge distillation for hyperspectral image classification," *IEEE Transactions on Geoscience and Remote Sensing*, vol. 63, pp. 1–15, 2025.
- [16] M. Ahmad, M. Usama, M. Mazzara, S. Distefano, H. A. Altuwaijri, and S. L. Ullo, "Fusing transformers in a tuning fork structure for hyperspectral image classification across disjoint samples," *IEEE Journal of Selected Topics in Applied Earth Observations and Remote Sensing*, vol. 17, pp. 18 167–18 181, 2024.
- [17] M. Ahmad, U. Ghous, D. Hong, A. M. Khan, J. Yao, S. Wang, and J. Chanussot, "A disjoint samples-based 3d-cnn with active transfer learning for hyperspectral image classification," *IEEE Transactions on Geoscience and Remote Sensing*, vol. 60, pp. 1–16, 2022.
- [18] B. Wang, X. Ping, and Y. Liu, "Hyperspectral system coupled with a global spectral feature classification network to identify the origin of mung bean," *Journal of Food Science*, vol. 91, no. 1, p. e70813, 2026. [Online]. Available: <https://ift.onlinelibrary.wiley.com/doi/abs/10.1111/1750-3841.70813>
- [19] T. Yang, S. Xiao, J. Qu, W. Dong, Q. Du, and Y. Li, "Graph embedding interclass relation-aware adaptive network for cross-scene classification of multisource remote sensing data," *IEEE Transactions on Image Processing*, vol. 33, pp. 4459–4474, 2024.
- [20] M. Ahmad, A. M. Khan, M. Mazzara, S. Distefano, S. K. Roy, and X. Wu, "Hybrid dense network with attention mechanism for hyperspectral image classification," *IEEE Journal of Selected Topics in Applied Earth Observations and Remote Sensing*, vol. 15, pp. 3948–3957, 2022.
- [21] M. Ahmad, M. Mazzara, S. Distefano, A. M. Khan, M. H. F. Butt, M. Usama, and D. Hong, "Graphmamba: Graph tokenization mamba for hyperspectral image classification," *IEEE Transactions on Emerging Topics in Computing*, vol. 13, no. 4, pp. 1510–1521, 2025.
- [22] A. Yang, M. Li, Y. Ding, L. Fang, Y. Cai, and Y. He, "Graphmamba: An efficient graph structure learning vision mamba for hyperspectral image classification," *IEEE Transactions on Geoscience and Remote Sensing*, vol. 62, pp. 1–14, 2024.
- [23] K. Sarpong, Z. Qin, R. Ssemwogerere, R. A. Patamia, A. M. Khamis, E. O. Gyamfi, F. Ekong, and C. C. Ukwuoma, "Hyperspectral image classification using second-order pooling with graph residual unit network," *Expert Systems with Applications*, vol. 238, p. 122202, 2024. [Online]. Available: <https://www.sciencedirect.com/science/article/pii/S0957417423027045>
- [24] M. Ahmad, M. Mazzara, S. Distefano, A. Mehmood Khan, M. Hassaan Farooq Butt, and D. Hong, "Policymamba: Localized policy attention with state space model for land cover classification," *IEEE Transactions on Neural Networks and Learning Systems*, vol. 36, no. 10, pp. 17 814–17 825, 2025.
- [25] S.-Y. Chen, K.-H. Hsu, and T.-H. Kuo, "Hyperspectral target detection-based 2-d-3-d parallel convolutional neural networks for hyperspectral image classification," *IEEE Journal of Selected Topics in Applied Earth Observations and Remote Sensing*, vol. 17, pp. 9451–9469, 2024.
- [26] H. Shi, Y. Zhang, G. Cao, and D. Yang, "Fortifying centers and edges: Multidomain feature learning meets hyperspectral image classification," *IEEE Transactions on Geoscience and Remote Sensing*, vol. 62, pp. 1–16, 2024.
- [27] M. Ahmad, U. Ghous, M. Usama, and M. Mazzara, "Waveformer: Spectral-spatial wavelet transformer for hyperspectral image classification," *IEEE Geoscience and Remote Sensing Letters*, vol. 21, pp. 1–5, 2024.
- [28] M. Ahmad, M. Usama, A. M. Khan, S. Distefano, H. A. Altuwaijri, and M. Mazzara, "Spatial-spectral transformer with conditional position encoding for hyperspectral image classification," *IEEE Geoscience and Remote Sensing Letters*, vol. 21, pp. 1–5, 2024.
- [29] Q. Wu, M. He, Q. Chen, L. Sun, and C. Ma, "Integrating multi-scale spatial-spectral shuffling convolution with 3d lightweight transformer for hyperspectral image classification," *IEEE Journal of Selected Topics in Applied Earth Observations and Remote Sensing*, pp. 1–17, 2025.
- [30] Y. Wang, L. Yang, T. X. Wu, K. Tang, and W. Zha, "Spatial-spectral fusion bifformer: A novel dynamic routing approach for hyperspectral image classification," *IEEE Transactions on Geoscience and Remote Sensing*, pp. 1–1, 2025.
- [31] Y. Fang, L. Sun, Y. Zheng, and Z. Wu, "Deformable convolution-enhanced hierarchical transformer with spectral-spatial cluster attention for hyperspectral image classification," *IEEE Transactions on Image Processing*, vol. 34, pp. 701–716, 2025.
- [32] B. Xi, Y. Zhang, J. Li, T. Zheng, X. Zhao, H. Xu, C. Xue, Y. Li, and J. Chanussot, "Mctgcl: Mixed cnn-transformer for mars hyperspectral image classification with graph contrastive learning," *IEEE Transactions on Geoscience and Remote Sensing*, vol. 63, pp. 1–14, 2025.
- [33] M. Ahmad, M. H. F. Butt, M. Usama, H. A. Altuwaijri, M. Mazzara, S. Distefano, and A. M. K. and, "Multi-head spatial-spectral mamba for hyperspectral image classification," *Remote Sensing Letters*, vol. 16, no. 4, pp. 339–353, 2025. [Online]. Available: <https://doi.org/10.1080/2150704X.2025.2461330>
- [34] X. Li, F. Xu, A. Yu, X. Lyu, H. Gao, and J. Zhou, "A frequency decoupling network for semantic segmentation of remote sensing images," *IEEE Transactions on Geoscience and Remote Sensing*, vol. 63, pp. 1–21, 2025.
- [35] Y. Rao, W. Zhao, Z. Zhu, J. Zhou, and J. Lu, "Gfnet: Global filter networks for visual recognition," *IEEE Transactions on Pattern Analysis and Machine Intelligence*, vol. 45, no. 9, pp. 10 960–10 973, 2023.
- [36] J. Lin, J. Chen, K. Yang, A. Roitberg, S. Li, Z. Li, and S. Li, "Adaptiveclick: Click-aware transformer with adaptive focal loss for interactive image segmentation," *IEEE Transactions on Neural Networks and Learning Systems*, vol. 36, no. 3, pp. 5759–5773, 2025.
- [37] D. Hong, Z. Han, J. Yao, L. Gao, B. Zhang, A. Plaza, and J. Chanussot, "Spectralformer: Rethinking hyperspectral image classification with transformers," *IEEE Transactions on Geoscience and Remote Sensing*, vol. 60, pp. 1–15, 2022.
- [38] R. Khan, T. Arshad, X. Ma, W. Chen, Z. Haifeng, and W. Yanni, "Deep spectral spatial feature enhancement through transformer for hyperspectral image classification," *IEEE Geoscience And Remote Sensing Letters*, 2024.
- [39] M. Ahmad, M. Usama, M. Mazzara, and S. Distefano, "Wavemamba: Spatial-spectral wavelet mamba for hyperspectral image classification," *IEEE Geoscience and Remote Sensing Letters*, vol. 22, pp. 1–5, 2025.
- [40] Y. Li, Y. Luo, L. Zhang, Z. Wang, and B. Du, "Mambahsi: Spatial-spectral mamba for hyperspectral image classification," *IEEE Transactions on Geoscience and Remote Sensing*, vol. 62, pp. 1–16, 2024.